Materials Horizons

ROYAL SOCIETY OF CHEMISTRY

COMMUNICATION

View Article Online
View Journal | View Issue

Cite this: *Mater. Horiz.*, 2025, **12**, 5175

Received 20th February 2025,
Accepted 11th April 2025

DOI: 10.1039/d5mh00302d

rsc.li/materials-horizons

A heterogeneous nanocomposite architecture with contrasting thermal conductivity and hydrophilicity for synergistic solar-thermal storage and evaporation†

Kit-Ying Chan,[ab] Xiuli Dong,[a] Yunfei Yang,[a] Xiaomeng Zhao,[a] Duo Li,[a] Mengyang Xu,[e] Xuemin Yin,[a] Zhenyu Wang[d] and Xi Shen *[abc]

Solar-driven evaporation is an eco-friendly and cost-effective freshwater production technique. It is essential to maintain continuous evaporation under intermittent sunlight for practical application. Integrating solar-thermal storage with evaporation is a promising solution. However, existing designs struggle to balance high evaporation rates with effective thermal energy storage in a single device due to conflicting thermal conductivity and hydrophilicity requirements for the two functions. Here, we develop a heterogeneous 3D graphene architecture featuring a hydrophilic gradient hydrogel evaporator (GHE) encircled by a hydrophobic thermal storage composite (TSC). The thermally conductive and hydrophobic TSC made from 3D graphene and paraffin wax enhances solar-thermal conversion and storage, while the thermally insulative and hydrophilic GHE featuring radiating channels with gradient pores facilitates efficient heat localization and water transport. This structurally and compositionally separated design leverages contrasting thermal and hydrophilic properties, achieving a high evaporation rate of 3.6 kg m^{-2} h^{-1} under direct sunlight and extending the evaporation at a rate of 2.7 kg m^{-2} h^{-1} for 30 minutes even when sunlight dims. The integrated device produces twice as much water as the hydrogel evaporator alone under intermittent lighting. This work presents an effective strategy for extending water generation capabilities under intermittent sunlight.

New concepts

This work demonstrates a new concept of a heterogeneous 3D graphene architecture that leverages structurally and compositionally distinct components to balance contrasting thermal conductivity and hydrophilicity requirements for synergistic solar-thermal storage and evaporation. The heterogeneous design featuring a hydrophilic gradient hydrogel evaporator (GHE) encircled by a hydrophobic thermal storage composite (TSC) allows us to achieve multifunctionality that would be challenging to realize in a single material. The GHE is tailored for efficient water transport and evaporation, while the TSC is optimized for thermal energy storage. Integrating these functionalities into a single material could compromise the performance of each function due to conflicting requirements for thermal conductivity and hydrophilicity. This work provides additional insights into multiscale structural design of the GHE and mechanistic understanding of thermal energy storage for enhanced evaporation under intermittent sunlight. The architecture of the GHE includes macroscale radiating gradient channels for efficient heat distribution, microscale aligned graphene oxide sheets for improved light-to-heat conversion, and nanoscale functional groups for enhanced hydrophilicity, as well as its effective integration with the TSC. We also quantified the contribution of additional power for evaporation due to thermal energy storage, underscoring the crucial role of the TSC in maintaining stable high performance under intermittent sunlight.

Introduction

Water scarcity is a threat to humanity worldwide, especially in developing countries and remote areas.[1,2] Solar-driven water evaporation is a promising freshwater generation technique by harvesting solar energy and converting it to heat using light-absorbing evaporators. These evaporators have been constructed from photothermal materials such as plasmonic nanoparticles,[3,4] graphene oxide (GO),[5,6] carbon nanotubes (CNTs)[7–9] and MXenes.[10,11] In addition to high solar absorption, a low thermal conductivity (k) for reduced heat loss and high hydrophilicity for fast water transport are required. In the past decade, myriad research efforts have been devoted to engineering solar evaporators for broadband solar absorption,[4,12,13] reduced heat losses,[14–16] and efficient water supply[17–19] for high-performance water evaporation. The construction of porous three-dimensional (3D) nanocomposite evaporators has been demonstrated as an

[a] *Department of Aeronautical and Aviation Engineering, The Hong Kong Polytechnic University, Hong Kong SAR, China. E-mail: xi.shen@polyu.edu.hk*
[b] *The Research Institute for Advanced Manufacturing, The Hong Kong Polytechnic University, Hong Kong SAR, China*
[c] *The Research Institute for Sports Science and Technology, The Hong Kong Polytechnic University, Hong Kong SAR, China*
[d] *School of Mechanical Engineering, Jiangnan University, Wuxi, China*
[e] *Department of Chemical and Biological Engineering, The Hong Kong University of Science and Technology, Hong Kong, China*

† Electronic supplementary information (ESI) available. See DOI: https://doi.org/10.1039/d5mh00302d

effective approach to achieve excellent thermal management, fast water transport, and high sunlight absorption simultaneously.[20,21] The rationally designed pore channels with different alignment structures,[10,22,23] *e.g.*, MXene/polyvinyl alcohol (PVA) aerogels with horizontal pore alignments, provided both a low k of 0.06 W m^{-1} K^{-1} and fast water transport, leading to a high evaporation rate of $\sim$2 kg m^{-2} h^{-1}.[10] Recently, hydrogel-based evaporators, such as hydrophilic PVA hydrogels, with a superior evaporation rate ($>$3 kg m^{-2} h^{-1}) have been developed by exploiting the abundant hydroxyl groups (–OH) in polymer networks,[24–26] despite having higher k compared to aerogel counterparts. Although the performance of water evaporation has been significantly improved by tailoring the composition and microstructure of evaporators, it remains a formidable challenge to translate these lab-scale evaporators into practical freshwater production devices. A primary challenge lies in the intermittent nature of sunlight in practical settings. Maintaining effective evaporation even during periods of reduced sunlight availability is a daunting task. Recent advancements have focused on integrating solar thermal evaporation setups with thermoelectric devices to simultaneously generate water and electricity.[27,28] This approach enhances overall energy utilization by converting excess thermal energy into electricity, which can be stored in batteries for use during periods without sunlight. However, the use of batteries can be challenging in harsh environmental conditions, including high humidity, saltwater exposure, and temperature fluctuations, which can lead to corrosion and reduced battery lifespan.

To address the challenges posed by intermittent sunlight and to complement battery usage, interfacial evaporators using phase-change material (PCM) microcapsules as solar absorbers have been developed.[29,30] The PCM microcapsule-based evaporation systems exhibited high evaporation rates of $\geq$2 kg m^{-2} h^{-1} under one sun. The PCM also stored thermal energy under sunlight and released it for evaporation when sunlight was absent, maintaining a high evaporation rate during illumination–dark cycles for continuous evaporation performance under solar irradiation interruptions. In addition to PCM microcapsules, a paraffin block was also integrated into the polypyrrole (PPy)-based evaporator to enhance the evaporation performance under intermittent solar irradiation.[31] However, the current design entails integrated evaporation and thermal energy storage functions using a single structure, by which it is difficult to achieve both high evaporation rate and energy storage capability, given the vastly different requirements in their hydrophilicity and thermal conductivities (k). Evaporators required highly hydrophilic structures.[23] However, the PCM microcapsules were hydrophobic, unable to deliver fast water transport. A cotton pad was used for water supply, which separated microcapsules and in turn led to a low k of the device. While low k was favorable for reduced heat loss in evaporation, thermal energy storage required high k to transfer the absorbed heat in the microcapsules for high thermal energy storage efficiency.[32] Integrated evaporation and thermal energy storage functions are challenging to achieve in a single device due to the conflicting hydrophilicity and k requirements.

Here, we developed an integrated solar-thermal storage and evaporation (ISTSE) device based on heterogeneous 3D graphene architectures to boost freshwater generation under intermittent sunlight, as shown in Fig. 1a. The ISTSE device comprised a hydrophilic gradient hydrogel evaporator (GHE) surrounded by a hydrophobic thermal storage composite (TSC) at the top, forming mushroom-like heterogeneous architectures for synergistic solar-thermal energy storage and evaporation (Fig. 1a and b). The GHE was made of PVA and GO due to their rich oxygen-containing functional groups, which enhance hydrophilicity and facilitate efficient water transport to the evaporation surface. This also enables the formation of stable hydrogels without the need for additional chemical crosslinkers, thereby simplifying the fabrication process and potentially reducing costs. In addition, the excellent light absorption properties of GO across a broad spectrum are crucial for converting solar energy into heat efficiently. For TSC, the graphene network is created using chemical vapor deposition (CVD), forming a highly conductive 3D structure that enhances heat conduction throughout the TSC. In addition, the excellent light absorption properties of graphene can contribute to effective solar-thermal conversion. CNTs act as a secondary conductive network, particularly effective in conducting heat within the larger pores of the graphene network, ensuring even heat distribution and minimizing thermal gradients. This synergy between graphene and CNTs maximizes the thermal management capabilities of the composite. Furthermore, paraffin wax (PW) is chosen for its high latent heat of fusion and reversible phase change, allowing it to absorb and release heat repeatedly without significant degradation over many cycles, which is crucial for the long-term reliability and efficiency of the TSC. The compositionally and structurally separated design allowed contrasting k values and hydrophilicity for the two functions. Under solar irradiation, the TSC was designed to efficiently store part of the thermal energy absorbed from the sun as latent heat while transferring the excessive heat to the hydrogel evaporator, giving rise to a high evaporation rate of 3.6 kg m^{-2} h^{-1} under one sun. More importantly, the stored thermal energy could be released once the sunlight was dimmed, maintaining freshwater generation over an extended period at an evaporation rate of 2.7 kg m^{-2} h^{-1} even after the sunlight was blocked. This work paves the way for high-performance freshwater generation under practical intermittent sunlight conditions by integrating thermal energy storage capability into solar evaporators.

Results and discussion

Heterogeneous design of 3D graphene architectures for ISTSE

The main challenges to integrating thermal energy storage capabilities with solar evaporators stem from the vastly different requirements for their k and hydrophilicity. Thermal energy storage requires a high k to facilitate fast charge–discharge cycles whereas a low k in the thickness direction is desired for solar evaporators to minimize the heat loss to bulk water. In the case of an integrated system, thermal energy generated and

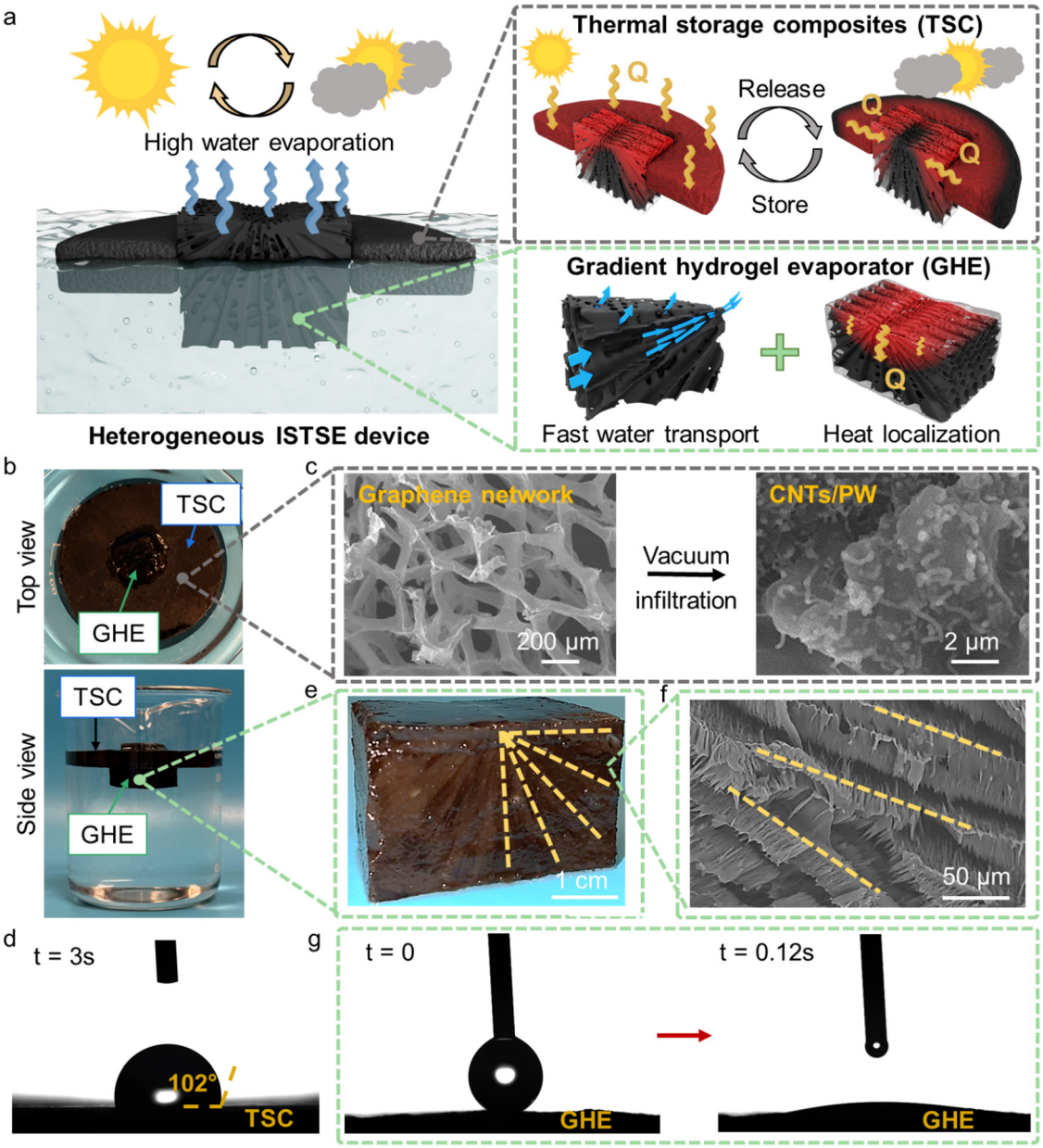

Fig. 1 Heterogeneous design of 3D graphene architectures for ISTSE. (a) Schematics of the ISTSE device consisting of TSC for thermal energy storage and release under intermittent solar irradiation and GHE with fast water transport ability and balanced thermal management. (b) Photographs showing the self-floating ability of the ISTSE device. (c) Scanning electron microscope (SEM) images showing the interconnected graphene network and CNTs/PW. (d) Optical image showing the water contact angle of TSC 3s after a water droplet is added. (e) A digital image showing the dark appearance and radiating gradient channels on the cross-section of GHE. (f) SEM image showing the gradient pores for water transportation. (g) Optical images showing the high hydrophilicity of GHE.

stored needs to be quickly transferred and distributed to the evaporation surface, calling for a high in-plane k on the evaporation surface and thus further complicating the structural design. Moreover, hydrophobic phase-change polymers used for thermal energy storage are not suited as evaporators, which require hydrophilic properties for water absorption. To tackle these challenges, we propose a heterogenous architecture consisting of a hydrophilic GHE surrounded by a hydrophobic TSC for synergistic solar-thermal energy storage and evaporation (Fig. 1a and b). The TSC was made from a thermally conductive, interconnected graphene network to host PW for solar-thermal conversion and storage (Fig. 1c). CNTs were incorporated into the PW to form dual thermally conductive networks for improved thermal storage efficiency and enhanced solar absorption. Both the carbon skeleton and PW were highly hydrophobic, giving rise to a water contact angle of 102° for TSC (Fig. 1d). The hydrophobic nature enabled self-floating of the ISTSE device on the water surface (Fig. 1b and Video S1, ESI†). Unlike the previous systems using phase-change microcapsules as both thermal energy storage and evaporators,[29,30] the GHE was

compositionally and structurally separated from the TSC such that contrasting *k* values and hydrophilicity could be attained for the two functions. The GHE was surrounded by the TSC at the top surface, featuring pore channels in a radiating pattern (Fig. 1e and f) with gradient pore sizes (Fig. S1, ESI†). The radiating channels allowed the heat released by the TSC to fast spread on the evaporating surface while suppressing the thermal conduction in the thickness direction to minimize heat losses to bulk water. Meanwhile, the gradient pores with reducing pore size from bottom to top facilitated fast water transport for evaporation. The GHE was made from hydrophilic GO and PVA, exhibiting almost instant water absorption after dispensing of a water droplet on the surface (Fig. 1g).

The above design encompassing functionally separated TSC and GHE aims to achieve several unique features for sustained water generation under intermittent sunlight. First, carbon-based TSC and GHE with different *k* values could efficiently convert and transfer heat for water generation while extra heat could be stored in the PW when sunlight was abundant. Second, when the solar irradiation was blocked by clouds, the stored heat could be released from TSC and effectively transferred to GHE to continuously drive the evaporation. Third, the hydrophilic GHE with gradient pore channels warranted fast water transport for water evaporation while the hydrophobic TSC was essential to keep the device afloat without extra support.

GO/PVA hydrogels for high evaporation performance

Pore morphology is an important factor determining the thermal and water transport in hydrogel evaporators. A conventional unidirectional freeze-casting method yielded vertical hydrogel evaporator (VHE) contains vertically aligned pores (Fig. 2a and Fig. S2, ESI†),[33–37] facilitating fast water transport but also exacerbating the heat loss to bulk water through vertical cell walls. Moreover, the in-plane *k* along the evaporation surface is rather low due to the transversely aligned pores,[38–40] unable to effectively transfer the heat from TSC to

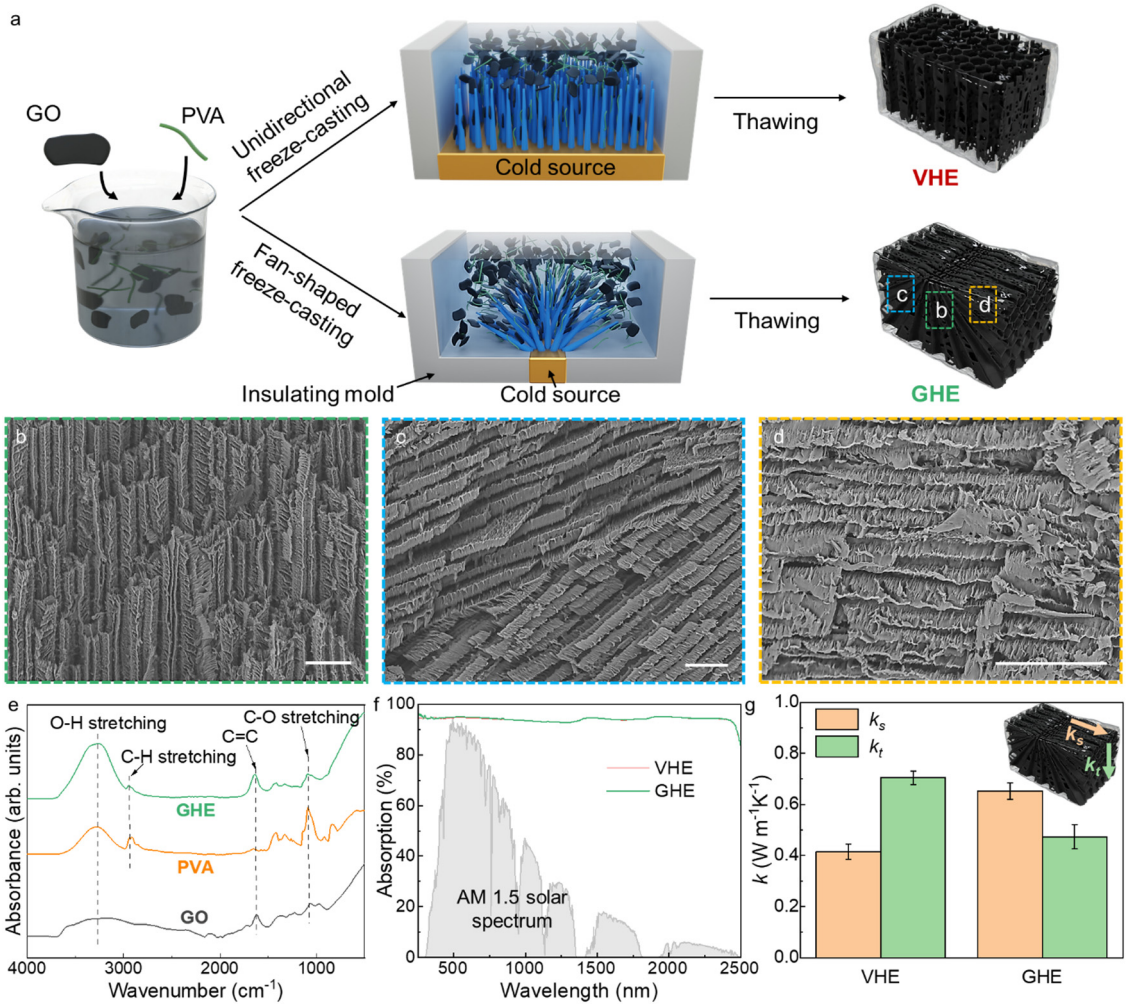

Fig. 2 Fabrication, structures, and thermal properties of GHE. (a) Schematics of the set-up and operating principles of the unidirectional and fan-shaped freeze-casting for VHE and GHE, respectively. SEM images showing the pore channels of GHE (b) vertically in the center, (c) radiating towards the edges and (d) horizontally on the evaporation surface. Scale bars: 100 μm. (e) The FTIR spectra of GHE, PVA and GO. (f) Solar absorption spectra and (g) anisotropic *k* values of VHE and GHE.

the entire evaporation surface. Here, we designed the GHE with pore channels arranged in a radiating pattern with gradient pore sizes to achieve the desired anisotropic heat transport without affecting the water transport. The GHE was fabricated from a GO and PVA mixture solution using a fan-shaped freeze-casting technique with a narrow metallic strip as the cold source at the bottom (Fig. 2a). The ice crystals nucleated favorably on the metallic strip and grew outwards in a radiating pattern with increasing separation between solidification fronts. The freeze-cast GO/PVA sample was thawed under ambient conditions after placing in a freezer at −40 °C overnight to allow physicochemical crosslinking between PVA chains.[41,42] The ambient-thawed sample was flipped upside down to obtain GHE for applications, exhibiting a dark color with radiating gradient channels (Fig. 1e). The scanning electron microscopy (SEM) images show that the pore channels were arranged vertically in the center (Fig. 2b). But turned increasingly slanted towards the edges (Fig. 2c), becoming almost horizontal on the evaporation surface (Fig. 2d). Moreover, the pore sizes were ~30 μm close to the bottom of GHE, narrowing down to only ~10 μm near the evaporation surface (Fig. S1, ESI†). The gradient structures can be controlled through different approaches such as tailoring the solid content in colloidal solution and freezing temperature for freeze-casting, as shown in Fig. S3 and S4 (details refer to Note S2, ESI†). The Fourier-transform infrared microscopy (FTIR) spectrum of GHE showed similar characteristic peaks as PVA except for a new peak at ~1650 cm^{-1} (Fig. 2e),[26] corresponding to the C=C bond stretching of the aromatic rings in GO.[43] This confirms the presence of GO in the PVA network, both of which were hydrophilic to the benefit of water absorption for evaporation. Indeed, the water content in the GHE was over 96 wt%

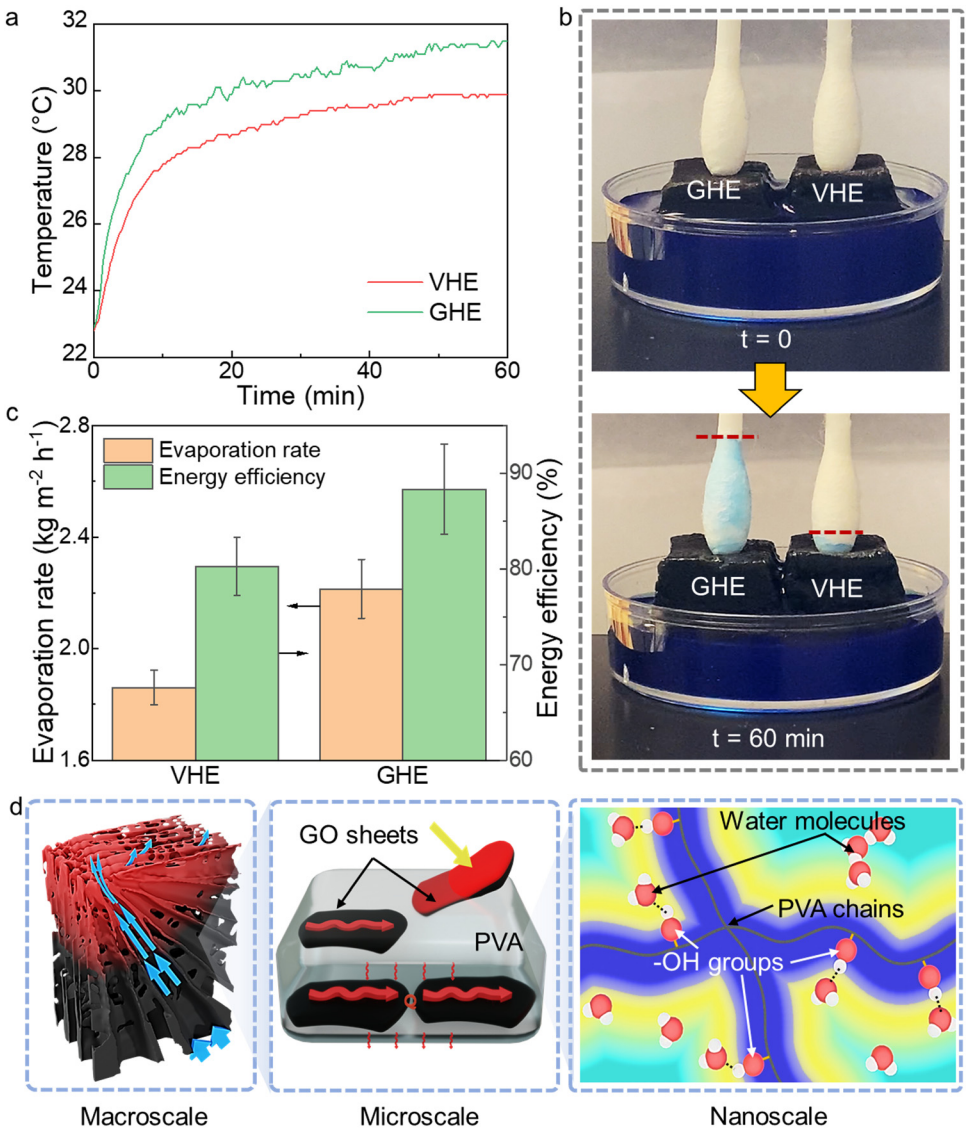

Fig. 3 Water evaporation performance of GHE under one-sun illumination. (a) Time-dependent surface temperatures of GHE and VHE under the solar intensity of 1 kW m^{-2}. (b) Digital images showing faster water transportation of GHE than VHE. (c) Evaporation rate and energy efficiency of GHE and VHE under the solar intensity of 1 kW m^{-2}. (d) Schematics of the multiscale structures responsible for excellent water evaporation performance of GHE.

(calculation refers to Note S3, ESI†) when saturated, confirming its strong water absorption capability.

To highlight the important role of radiating channels in thermal management, the optical and thermal properties of GHE were compared to the VHE with the same composition. Thanks to the highly porous structures, both VHE and GHE exhibited almost the same, high solar-weighted absorption of 94% (Fig. 2f). However, GHE and VHE had distinct anisotropic k arising from their microstructures (Fig. 2g). Due to the vertically aligned pore channels, VHE had a higher k in the thickness direction (k_t) than that along the evaporation surface (k_s). The high k_t of 0.71 W m^{-1} K^{-1}, even higher than that of water (0.6 W m^{-1} K^{-1}), led to considerable heat loss from the evaporation surface to bulk water. Meanwhile, the relatively low k_s of 0.41 W m^{-1} K^{-1} could limit the heat transfer from the side to the center of evaporation surface when integrated with the TSC. By contrast, GHE with pores aligned in the radiating pattern showed a 59% higher k_s (0.65 W m^{-1} K^{-1}) while 34% lower k_t (0.47 W m^{-1} K^{-1}) than VHE. The high k_s was attributed to the horizontally aligned pore channels on the surface, promoting heat conduction from the surrounding TSC to the evaporation surface. The low k_t arose from the slanted cell walls, blocking the heat loss from the evaporation surface to bulk water. To summarize, the anisotropic k of GHE favored the fast heat conduction along the evaporation surface to uniformly distribute the heat generated from the surrounding TSC, while minimizing the heat loss to bulk water by virtual of its low k_t.

The lower heat loss of GHE led to a better thermal management than conventional VHE during evaporation. As shown in Fig. 3a, the surface temperature of GHE reached 32 °C, 2 °C higher than that of VHE under one sun. In addition, thanks to the hydrophilic GO/PVA networks and gradient structures, the GHE demonstrated faster water uptake than VHE (Fig. 3b and Video S2, ESI†). The lower heat loss together with better water transport eventually translated into a higher water evaporation rate of GHE than VHE under solar irradiation. The mass of water reduced much faster for GHE than VHE under one sun (Fig. S5a, ESI†), resulting in a high evaporation rate of 2.2 kg m^{-2} h^{-1} for GHE, 16% higher than that of VHE (Fig. 3c). The corresponding solar-to-vapor energy efficiency, η, was calculated as follows:

$$\eta = \frac{\dot{m} h_v}{C_{opt} P_0}, \quad (1)$$

where $\dot{m}$ is the evaporation rate after subtracting dark evaporation (Fig. S5b, ESI†), h_v is the equivalent enthalpy of vaporization, which is estimated from the dark evaporation rate (Fig. S5c, ESI†), C_{opt} is the optical concentration on the sample surface and P_0 is the solar irradiation power. The energy efficiency of GHE was 88.3%, 10% higher than VHE (Fig. 3c). These results highlight the positive role of multiscale structures responsible for excellent water evaporation performance of GHE (Fig. 3d). In the macroscale, the radiating gradient channels balanced the heat conduction on the evaporation surface and thermal insulation in the thickness direction, while the gradient pore sizes promoted water transport in the GHE. In the microscale, the presence of horizontally aligned GO sheets at the surface promotes the heat conduction in a desired direction, further optimizing the balanced thermal management, in addition to its excellent solar-to-heat conversion performance. In the nanoscale, the abundant oxygen-containing functional groups also enhance the hydrophilicity of GHE, translating into fast water transport performance. In addition, the long-term stability of GHE was also demonstrated through 50-cycle evaporation tests under one sun (Fig. S6a, ESI†). The structural and chemical stability of GHE was further confirmed by FTIR (Fig. S6b, ESI†) and SEM analyses (Fig. S6c and d, ESI†), respectively.

TSC for thermal energy storage

The other functional component in the ISTSE device is the TSC. Thermal energy storage materials require a high k value for fast charge and discharge, in stark contrast to the low k requirement for solar evaporators. Furthermore, common PCMs for thermal energy storage are mostly highly hydrophobic, requiring analogously hydrophobic skeletons to host them, which is opposed to the hydrophilic requirement for solar evaporators. The reported integrated devices normally utilized a single material for both thermal energy storage and evaporation,[29–31] unable to reconcile the contrasting demands for k and hydrophilicity. Here, we designed a TSC, which was compositionally different and structurally separated from the GHE, as the solar-thermal energy storage component, aiming to achieve a high k value for fast charging and discharging. The TSC contained a 3D CVD-grown interconnected graphene skeleton, which was further infiltrated with CNTs/PW composites (Fig. 1c). Unlike the abundant hydroxyl functional groups in GO and PVA used in GHE, both the CVD-grown graphene and CNTs in TSC contained much fewer oxygen-containing functional groups (Fig. S7, ESI†),[44] making the TSC highly hydrophobic with a water contact angle of 102° (Fig. 1d and Fig. S8, ESI†). The hydrophobic TSC encircled the hydrophilic GHE, enabling the self-floating ability of the integrated device without extra support (Fig. 1b). Without the TSC, GHE alone sank to the bottom when placed on water because of its hydrophilicity (Fig. S9, ESI†). Moreover, the CVD-grown graphene had few structural defects as indicated by the low Raman D to G peak intensity ratios of ~0.23 (Fig. S10, ESI†), beneficial to a much higher k than GO.[45,46] Together with the dual conductive network created by CNTs, the TSC achieved a much higher k value of 1.27 W m^{-1} K^{-1} than its GHE counterpart (0.65 and 0.47 W m^{-1} K^{-1} in the evaporation surface and thickness directions, respectively). This high k was a significant 390% improvement against pristine PW (0.26 W m^{-1} K^{-1}), as presented in Fig. S11a (ESI†). It should also be noted that the improvement in k was attained at a low graphene and CNT loading of 6.5 wt% (Fig. S11b, ESI†), which ensured a minimum impact on the melting and crystallization temperatures, as well as the phase change enthalpy of PW. This negligible impact was confirmed by the almost identical differential scanning calorimetry (DSC) curves of TSC and PW, as shown in Fig. 4a. The DSC curves of TSC and PW showed two peaks at ~30 and ~50 °C, corresponding to the solid–solid phase transition and

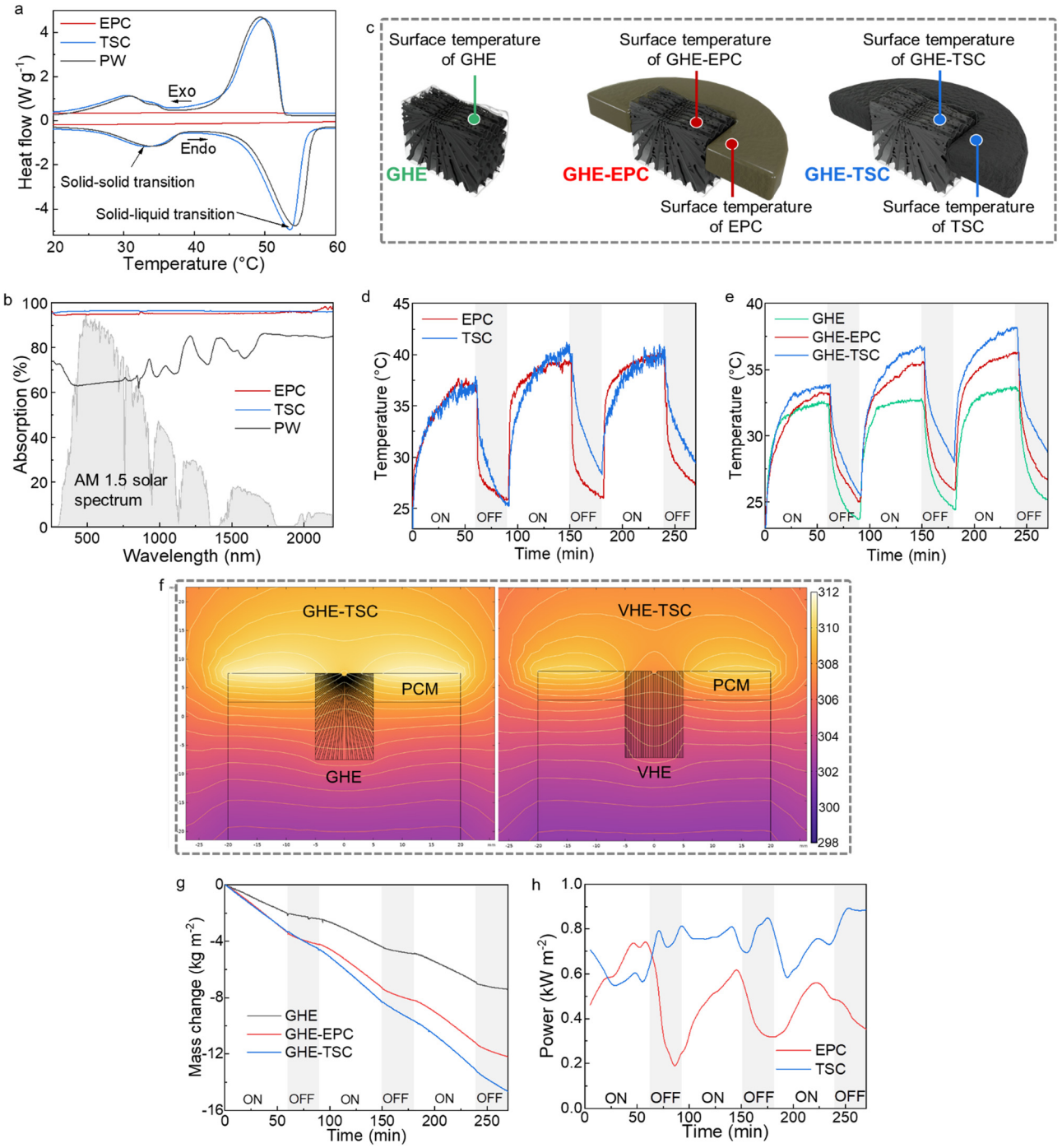

Fig. 4 Integration of TSC into GHE and freshwater generation performance under intermittent illumination–dark cycles. (a) DSC and (b) solar absorption spectra of EPC, TSC and PW. (c) Schematic illustrations showing the sample of GHE alone and the devices of GHE-EPC and GHE-TSC, and at which point different temperatures were measured in (d) and (e). (d) Temperature profiles of EPC and TSC. (e) Temperature profiles of GHE, GHE-EPC and GHE-TSC. (f) Temperature distribution and isotherm patterns for GHE-TSC and VHE-TSC after 60 minutes of illumination. (g) Mass changes of three evaporators during three illumination–dark cycles under one sun. (h) Extra powers provided by EPC and TSC to GHE for additional water production during three illumination–dark cycles under one sun.

solid–liquid phase change of PW, respectively.[47] The latent heats of melting and crystallization of the TSC were measured from the DSC curves as 180 and 175 J g^{-1}, respectively. These values were 94.2% and 92.1% of the corresponding latent heats of pristine PW (Fig. S11c, ESI†), indicating an excellent thermal energy storage capacity of TSC almost identical to pure PW despite the presence of graphene and CNTs. The solid–solid and solid–liquid phase change enthalpy of TSC are ~30 and ~150 J g^{-1} (Fig. S11d, ESI†), respectively. In addition to thermal conductivity and thermal energy storage capacity, light

absorption is also essential to solar-thermal energy storage. The pristine PW had a low optical absorption of ~70% in the solar wavelengths (Fig. 4b), which was ineffective to convert the solar energy to heat. The presence of graphene and CNTs greatly improved the solar absorption to ~96% thanks to the excellent photothermal effects of nanocarbons and abundant graphene/PW and CNTs/PW interfaces with mismatched refractive indices to promote extensive light scattering. It is also noted that the sunlight absorption of TSC was slightly higher than GHE, serving as additional heat source under sunlight to allow more effective utilization of solar energy.

Integration of GHE and TSC for freshwater generation under intermittent sunlight

Given the desired evaporation performance of GHE and thermal energy storage performance of TSC, we further integrate them into a GHE-TSC structure by encircling TSC around the top of GHE (Fig. 1a) to boost water generation under intermittent sunlight. To pinpoint the essential role of thermal energy storage on the water evaporation performance, we also prepared a control sample of the epoxy composite (EPC) in place of TSC in the integrated device for comparison. The EPC was made by replacing PW in the TSC with epoxy, showing no peaks in the DSC curve (Fig. 4a) and thus indicating its inability to store thermal energy. In addition, EPC exhibited a solar absorption comparable to TSC (Fig. 4b) because of their identical carbon networks. Therefore, a comparison between GHE-TSC and GHE-EPC can single out the contribution of thermal energy storage of TSC on the water production rate.

To evaluate the evaporation performance under intermittent sunlight, evaporation tests for three samples, GHE, GHE-EPC, and GHE-TSC (as illustrated in Fig. 4c), were carried out under repeated illumination–dark cycles. Each cycle comprised an illuminating period with an irradiation intensity of 1 kW m^{-2} for 60 min followed by a dark period (*i.e.*, with irradiation turned off) of 30 min. The test setup was placed in an environmental chamber covered by a blackout curtain. As a result, the solar intensity was very low, measured to be between 2 to 4 W m^{-2}, which can be considered negligible when sunlight dims. Such cycles mimic a cloudy weather condition where the sunlight is periodically blocked by moving clouds. The surface temperatures of EPC and TSC behaved differently because of the thermal energy storage capability of TSC, as shown in Fig. 4d. The surface temperatures of both TSC and EPC reached ~37.5 °C for the first illuminating cycle because of their almost identical solar absorption. When the light was turned off, the surface temperature of EPC dropped instantly to ~28 °C in only 5 min, while the cooling rate of TSC was much slower than EPC due to the latent heat release from PW. The latent heat storage and release behaviors of TSC were more evident in the second and third cycles, where the phase change became more stable. Once the irradiation was turned off in the second cycle, the temperature of EPC rapidly dropped from 39 to 28 °C in 10 min and then slowly returned to room temperature at the end of the second cycle. By contrast, the TSC held its surface temperatures better than EPC with a lower temperature decline rate of ~0.4 °C min^{-1} thanks to the latent heat release from the PW when temperatures dropped to its solid–solid phase transition region at around 38 °C. The latent heat released counterbalanced the fast temperature decay due to heat loss to the environment when the illumination was off, holding the temperature of TSC at 28.5 °C even at the end of the 30-min dark cycle.

The better temperature preserving ability of TSC directly translated into a higher evaporation surface temperature in the GHE–TSC than EPC–TSC systems under intermittent illumination. The evaporation surface temperatures (*i.e.*, the surface temperatures of GHE) of the three systems are compared in Fig. 4e. TSC and EPC with excellent photothermal conversion served as an additional heat source when encircling the GHE, raising the evaporation surface temperature of GHE to 34 and 33 °C in GHE–TSC and GHE–EPC, respectively, higher than the GHE acting alone (~32 °C) under illumination in the first cycle. For GHE–EPC, no additional heat was supplied to GHE in the dark period as indicated by the similar fast temperature decay when illumination was turned off. By contrast, TSC was able to provide additional heat through latent heat release to the evaporation surface in GHE–TSC even in the dark period, as demonstrated by the lower temperature reduction rate than GHE and GHE–EPC. This maintained the evaporation surface temperature of GHE–TSC over the illumination and dark periods at 34.2 and 30.4 °C on average, respectively, higher than its counterparts (Fig. S12, ESI†).

To understand the mechanism for maintaining high evaporation surface temperatures under both illumination and dark conditions, we carried out numerical simulations of thermal transport and phase change processes in the integrated devices (Note S5 and Fig. S13, ESI†). Under illumination, the surface temperature of TSC was higher than that of GHE (Fig. 4f and Fig. S13a, ESI†), which aligns with the experimental observations (Fig. S14, ESI†). This temperature difference was primarily due to graphene and CNTs exhibiting superior photothermal effects compared to GO and the absence of an evaporative cooling process for TSC. Consequently, under illumination, heat was transferred from TSC to GHE. The heat transfer from TSC to GHE was more effective than that from TSC to VHE, as evidenced by the more uniform temperature distribution (Fig. 4f) and smaller temperature difference between the two in the former (Fig. S13 and S14, ESI†). The in-plane aligned pores on the surface of GHE allowed the fast transfer of heat from periphery to center, while the slanted pores prohibited the heat dissipation along the thickness direction. Under the dark conditions, the energy stored in TSC was released to GHE through the same heat transfer mechanism as that under illumination, resulting in an apparent slow decay in temperature (Fig. S13, ESI†). In comparison, the EPC could not generate heat in the dark, giving rise to a sharp reduction in temperature (Fig. 4d and Fig. S13c, ESI†). These simulation results revealed the key role of radiating pore channels of GHE in anisotropic heat transfer for superior thermal management and its effective integration with TSC for maintaining the evaporation surface temperature during both illuminated and dark periods.

The mass changes of water during the cyclic illumination–dark tests using the three structures as evaporators are compared in Fig. 4g. It should be noted that TSC served as a thermal storage and supply component, storing solar energy and releasing it to GHE to support continuous evaporation, especially under intermittent sunlight. Since no evaporation occurred on the surface of TSC, only the surface area of GHE, where active evaporation takes place, was considered when calculating the evaporation rate of integrated device. Initially, steeper slopes were observed for GHE–TSC and GHE–EPC compared to GHE, suggesting higher evaporation rates of the formers thanks to the higher surface temperatures arising from better solar absorption of TSC and EPC. After the illumination was turned off, the water continued to be generated at a high rate of 2.7 kg m^{-2} h^{-1} for GHE–TSC, maintaining at ~75% of that under illumination because of the latent heat release. By contrast, the evaporation rate in GHE–EPC was reduced by half under dark as indicated by a plateau in the mass reduction curve due to the lack of energy storage capability. At the end of three cycles, the total water yield of GHE–TSC reached 14.6 kg m^{-2}, which was 20% higher than that of GHE–EPC (12.2 kg m^{-2}) and almost double that of GHE (7.4 kg m^{-2}). The major difference in the evaporation performance arose when the illumination was turned off (Fig. S15, ESI†). Although the structural and chemical separation of the ISTSE minimizes direct chemical bonds between its components, maintaining strong physical contact is essential. The compressible hydrogel is intentionally designed to be slightly larger than the opening in the TSC, ensuring a snug fit that enhances mechanical interlocking. This tight fit maximizes the surface area for heat exchange, thereby improving thermal conductivity across the interface and maintaining structural integrity. Consequently, the latent heat released from the TSC can be effectively transferred to the GHE, maintaining a high evaporation rate of 2.7 kg m^{-2} h^{-1} during the dark cycles, which was 54% and 246% higher than that of GHE–EPC and GHE, respectively. It is worth noting that this high evaporation rate of GHE–TSC achieved under dark conditions was even higher than that of GHE under illumination, demonstrating the effectiveness of GHE–TSC for extending the water production to the weather condition with intermittent sunlight. The evaporation efficiency of the GHE–TSC under intermittent illumination was determined to be ~200%. This was 114% higher than that of the GHE alone, which has an efficiency of ~95%. The significantly enhanced energy efficiency exceeding 100% for the GHE–TSC was due to the presence of the TSC, which released the stored energy during periods without direct solar input, providing additional heat to the GHE. This process effectively increased the total evaporation without requiring additional energy input, demonstrating the effectiveness of thermal storage to optimize energy utilization. To quantify the contribution of thermal energy storage to the evaporation, extra powers provided by TSC to GHE for evaporation were calculated during the illumination–dark cycles, as shown in Fig. 4h. The extra power provided by EPC was also calculated for the benchmark, which increased over time during illumination but dropped significantly once the illumination was turned off due to lack of thermal energy storage capability. In contrast, TSC provided a more stable and higher power supply to GHE for evaporation throughout the cyclic illumination–dark tests, highlighting the important role of thermal energy storage in maintaining stable high performance for evaporation under intermittent sunlight.

The above performance was achieved under a standard 1-sun irradiation, which increased the temperature of TSC up to 40 °C (Fig. 4d), allowing only solid–solid phase transition of PW with a transition temperature of ~34 °C (Fig. 4a). Although the latent heat storage capacity was limited under 1 sun because solid–solid phase transition constituted an enthalpy of only 30 J g^{-1}, the absence of solid–liquid phase transition was favorable to avoid leakage of melting PW and large volume change, achieving highly stable thermal energy storage and release over 10 repeated cycles (Fig. S16, ESI†). Nonetheless, concentrated sunlight can be used when high water production rate is required to increase the temperature of TSC over the solid–liquid phase transition temperature of ~54 °C (Fig. 4a) so that the total phase change enthalpy of ~180 J g^{-1} can be fully utilized. As a demonstration, the evaporation performance of GHE–TSC under 2-sun illumination was also studied and compared with that under 1 sun for the same three illumination–dark cycles (Fig. S17, ESI†). The surface temperature of TSC grew much faster under 2 suns than 1 sun, exhibiting a distinct variation in the slope between approximately 47 and 54 °C because of the solid–liquid phase change of PW, and ultimately reaching ~65 °C after 60-min illumination (Fig. S17a, ESI†). Upon cooling, the temperature profile also showed a change in slope from 49 to 44 °C corresponding to the thermal energy release associated with the solidification of PW. The temperature returned to 38 °C at the end of the first cycle, elevating the highest and lowest temperatures of the subsequent cycles. The high temperatures of TSC especially maintained in the dark period directly translated into the high evaporation surface temperatures (Fig. S17b, ESI†). The surface temperature of GHE increased up to ~50 °C under two suns for the second and third cycles and maintained well over 30 °C with obvious arrests in temperature drops even in the dark condition. Such high surface temperatures led to significantly improved evaporate rates of 5.8 kg m^{-2} h^{-1} and 3.6 kg m^{-2} h^{-1}, under illumination and dark conditions, respectively, when compared to those under one-sun (Fig. S18a and b, ESI†). To highlight the freshwater production under real intermittent sunlight exposure, the evaporation performance of the ISTSE device was also evaluated under the solar irradiation of 0.5 sun across three consecutive light on and off cycles (Fig. S18a and b, ESI†). At 0.5 sun, the evaporation rate of GHE–TSC was 2.3 kg m^{-2} h^{-1}. After the light was turned off for 30 minutes, the average evaporation rate was 1.9 kg m^{-2} h^{-1}. These results demonstrate that even under reduced sunlight exposure (0.5 sun), significant evaporation occurs, supporting the feasibility of freshwater production under real-world conditions where sunlight exposure may be intermittent or less intense.

The ISTSE device demonstrated a stable evaporation rate of ~3.5 kg m^{-2} h^{-1} during 24-hour continuous seawater evaporation, with no salt crystals forming on the evaporation surface as

shown in Fig. S19a (ESI†). This indicates effective desalination and evaporation performance. The salt rejection mechanism, which involves enhanced downward ion transport due to the gradient pore channels, was discussed in detail in our previous study.[23] In addition, the concentrations of various ions in seawater before and after desalination were measured (Fig. S19b, ESI†), confirming the high quality of the condensed water. This suggests that the device effectively removes salts and impurities from seawater. The potential material degradation mechanism could include UV degradation due to prolonged exposure to sunlight and fatigue resulting from mechanical stress caused by thermal expansion and contraction during day and night cycles.

Outdoor water evaporation tests

We performed outdoor tests to further evaluate the thermal storage performance of TSC and its effect on the water production under realistic weather conditions. As shown in Fig. S20 (ESI†), two experimental setups, one contained GHE and the other being the ISTSE device made from GHE–TSC, were placed next to each other for testing in an open area at Hung Hom,

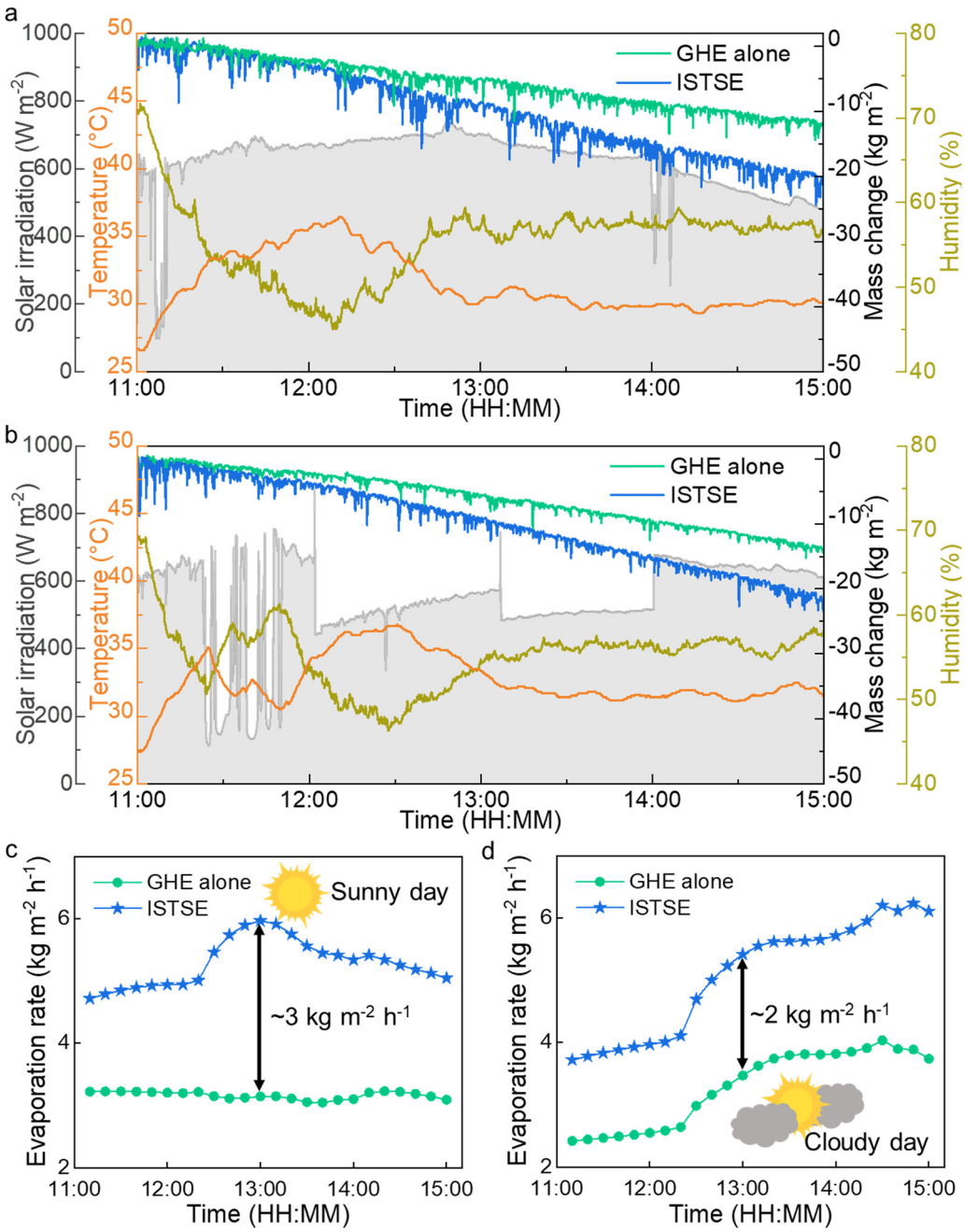

Fig. 5 Outdoor performance of ISTSE on both sunny and cloudy days. Mass changes of water using GHE and ISTSE as evaporators, solar irradiation, ambient temperature, and humidity on (a) a sunny day on 2nd November 2023 and (b) a cloudy day on 3rd November 2023, in Hong Kong, China. Evaporation rates of GHE alone and ISTSE on (c) sunny day and (d) cloudy day, respectively.

Hong Kong, on both a sunny day (2nd November 2023) and a cloudy day (3rd November 2023) from 11:00 a.m. to 3:00 p.m. To minimize the effect of wind and heat loss, wind shields and thermal insulation were applied. It should be noted that temperature and humidity significantly influence the evaporation performance, which is a diffusion process driven by the vapor concentration difference between the evaporation surface and ambient air. A higher temperature and higher relative humidity can lead to a higher actual vapor density in the air, significantly slowing down the evaporation process since the water vapor concentration difference between the evaporation surface and ambient air is reduced. In addition, the air movement (*e.g.* wind in outdoor experiments) can remove the saturated layer of water vapor above the evaporation surface, further promoting the evaporation and leading to a much higher evaporation rate.

On the sunny day, the ISTSE device exhibited a total water generation of $\sim$20 kg m^{-2}, 71% higher than that generated by the GHE alone, as shown in Fig. 5a. On the cloudy day, the solar irradiation was intermittent (Fig. 5b). Nonetheless, the ISTSE device still achieved a water generation of $\sim$21 kg m^{-2}, 58% higher than the GHE alone. Fig. 5c shows a higher water evaporation rate of the ISTSE device compared to the GHE alone on the sunny day, with a maximum rate difference of $\sim$3 kg m^{-2} h^{-1}, due to the additional heat source from TSC to GHE under solar irradiation. Even under cloudy conditions, the ISTSE device also exhibited a $\sim$2 kg m^{-2} h^{-1} higher evaporation rate than GHE alone (Fig. 5d). The outdoor tests demonstrated superior performance of the ISTSE device over the GHE alone under both sunny and cloudy conditions. An additional outdoor test was conducted to evaluate and compare the water evaporation performance of GHE–EPC and GHE–TSC (Fig. S21, ESI†). The evaporation rate of GHE–TSC was lower than that of GHE–EPC before 12:30 p.m. (Fig. S21b, ESI†). This is likely because the TSC stored part of the absorbed thermal energy as latent heat, resulting in a smaller increase in the evaporation rate of GHE in the GHE–TSC device compared to the GHE–EPC device. Once the solid–solid transition in the TSC was completed, the evaporation rate of GHE–TSC increased, as no additional energy was required for latent heat storage, allowing all extra heat to be directed to the GHE for enhanced water evaporation. Notably, the evaporation rate of GHE–TSC surpassed that of GHE–EPC when the ambient temperature dropped (Fig. S21a, ESI†), indicating that latent heat release helped maintain the high evaporation rate of GHE–TSC.

To assess the practical versatility of the ISTSE device, a steam generation chamber containing the ISTSE device for water collection was placed outdoors from 10:40 a.m. to 6:00 p.m. on 25th March 2025 (Fig. S22a, ESI†). Under direct sunlight, vapor was generated and condensed on the inner surface of the chamber, as illustrated in Fig. S22b (ESI†). The condensed droplets were subsequently collected through the chamber's bottom outlet. After $\sim$7 hours of sunlight exposure, the cumulative water production was about 13 kg m^{-2} (Fig. S22c, ESI†), resulting in an average water collection rate of 1.8 kg m^{-2} h^{-1}, demonstrating a significant potential for freshwater generation.

Conclusions

In summary, we developed a heterogeneous 3D graphene architecture featuring structurally and functionally distinct TSC and GHE with contrasting k and hydrophilicity for integrated solar-thermal storage and evaporation. The TSC, featuring a thermally conductive network of interconnected graphene and CNTs, achieves an enhanced thermal conductivity of 1.27 W m^{-1} K^{-1} and impressive solar absorption of approximately 96%. The carbon framework and PW within the TSC are highly hydrophobic, resulting in a water contact angle of 102°. In contrast, the GHE exhibits varied thermal conductivities of 0.65 W m^{-1} K^{-1} on the evaporation surface and 0.47 W m^{-1} K^{-1} in the thickness direction. This design, featuring radiating pore channels, allows heat released by the TSC to rapidly disperse across the evaporating surface while minimizing thermal conduction through the thickness, thereby reducing heat loss to the bulk water. The hydrophilic GHE ensured rapid water transport, while the hydrophobic TSC kept the device afloat. Thanks to their contrasting k values, the TSC efficiently converted solar energy into heat and transferred it to the GHE for water generation. This resulted in an evaporation rate of 3.6 kg m^{-2} h^{-1} under one sun. Notably, the TSC stored excessive heat during illumination periods. This stored thermal energy was then released during dark periods, maintaining a consistent and high evaporation rate of 2.7 kg m^{-2} h^{-1} solely relying on the heat released from the TSC. Over three illumination-dark cycles, the ISTSE device produced 14.6 kg m^{-2} of water, nearly doubling the output of the hydrogel evaporator alone. Our work highlights the potential of integrating thermal energy storage into solar evaporators, enabling sustained freshwater generation under realistic intermittent sunlight conditions.

Author contributions

Kit-Ying Chan: conceptualization, data curation, formal analysis, methodology, writing – original draft. Xiuli Dong: data curation; methodology. Yunfei Yang: data curation; methodology. Xiaomeng Zhao: methodology. Duo Li: methodology. Mengyang Xu: methodology. Xuemin Yin: methodology. Zhenyu Wang: writing – review & editing. Xi Shen: conceptualization; supervision; writing – review & editing.

Data availability

The data supporting this article have been included as part of the ESI.† Further relevant data are available from the corresponding author upon reasonable request.

Conflicts of interest

The authors declare no conflict of interest.

Acknowledgements

This project was financially supported by the Young Scientists Fund of National Natural Science Foundation of China (Grant No. 52303106), the Research Grants Council of Hong

Kong SAR (16200720), the Environment and Conservation Fund of Hong Kong SAR (Project No. ECF 21/2022), the Research Institute of Sports Science and Technology (Project No. P0043535), and the start-up fund for new recruits of PolyU (Project No. P0038855 and P0038858). K. Y. Chan acknowledges funding support from the Young Scientists Fund of National Natural Science Foundation of China (Grant No. 52303351), the Environment and Conservation Fund of Hong Kong SAR (Project No. ECF 54/2023), the Research Institute of Advanced Manufacturing (Project No. P0046125), and the start-up fund for new recruits of PolyU (Project No. P0044127).

References

1 X. Li, X. Min, J. Li, N. Xu, P. Zhu, B. Zhu, S. Zhu and J. Zhu, *Joule*, 2018, **2**, 2477–2484.
2 C. He, Z. Liu, J. Wu, X. Pan, Z. Fang, J. Li and B. A. Bryan, *Nat. Commun.*, 2021, **12**, 4667.
3 Y. Wang, H. Ma, J. Yu, J. Li, N. Xu, J. Zhu and L. Zhou, *Adv. Opt. Mater.*, 2023, **11**, 2201907.
4 L. Zhou, Y. Tan, J. Wang, W. Xu, Y. Yuan, W. Cai, S. Zhu and J. Zhu, *Nat. Photonics*, 2016, **10**, 393–398.
5 C. T. K. Finnerty, A. K. Menon, K. M. Conway, D. Lee, M. Nelson, J. J. Urban, D. Sedlak and B. Mi, *Environ. Sci. Technol.*, 2021, **55**, 15435–15445.
6 Y. Li, T. Gao, Z. Yang, C. Chen, Y. Kuang, J. Song, C. Jia, E. M. Hitz, B. Yang and L. Hu, *Nano Energy*, 2017, **41**, 201–209.
7 P. Cao, L. Zhao, J. Zhang, L. Zhang, P. Yuan, Y. Zhang and Q. Li, *ACS Appl. Mater. Interfaces*, 2021, **13**, 19109–19116.
8 N. Hu, S. Zhao, T. Chen, X. Lu and J. Zhang, *ACS Appl. Mater. Interfaces*, 2022, **14**, 46010–46022.
9 L. Zhao, Z. Yang, J. Wang, Y. Zhou, P. Cao, J. Zhang, P. Yuan, Y. Zhang and Q. Li, *J. Chem. Eng.*, 2023, **451**, 138676.
10 H. Zhang, X. Shen, E. Kim, M. Wang, J. H. Lee, H. Chen, G. Zhang and J. K. Kim, *Adv. Funct. Mater.*, 2022, **32**, 2111794.
11 B. Zhang, P. W. Wong and A. K. An, *J. Chem. Eng.*, 2022, **430**, 133054.
12 Y. Liu, J. Zhao, S. Zhang, D. Li, X. Zhang, Q. Zhao and B. Xing, *Environ. Sci.:Nano*, 2022, **9**, 2264–2296.
13 J. Zhu, X. Wang, J. Liang, X. Qiu, S. Chen, Y. Wang and Y. Wang, *EcoMat*, 2023, **5**, e12323.
14 Y. G. F. Zhao, X. Zhou, W. Shi and G. Yu, *Nat. Rev. Mater.*, 2020, **5**, 388–401.
15 Y. Wang, C. Wang, X. Song, M. Huang, S. K. Megarajan, S. F. Shaukat and H. Jiang, *J. Mater. Chem. A*, 2018, **6**, 9874–9881.
16 J. Sun, R. Teng, J. Tan, M. Xu, C. Ma, W. Li and S. Liu, *J. Mater. Chem. A*, 2023, **11**, 6248–6257.
17 Y. Sun, X. Zong, D. Qu, G. Chen, L. An, X. Wang and Z. Sun, *J. Mater. Chem. A*, 2021, **9**, 7122–7128.
18 Z. Wang, X. Wu, F. He, S. Peng and Y. Li, *Adv. Funct. Mater.*, 2021, **31**, 2011114.
19 X. Wang, Z. Huang, D. Miao, J. Zhao, J. Yu and B. Ding, *ACS Nano*, 2018, **13**, 1060–1070.
20 X. Zhang, J. Liu, S. Han, W. Li, C. Li, F.-L. Gao, C. Shu, Z.-Z. Yu and X. Li, *ACS Appl. Mater. Interfaces*, 2023, **15**, 51289–51299.
21 L. Pu, H. Ma, J. Dong, C. Zhang, F. Lai, G. He, P. Ma, W. Dong, Y. Huang and T. Liu, *Nano Lett.*, 2022, **22**, 4560–4568.
22 W. Xu, Y. Xing, J. Liu, H. Wu, Y. Cui, D. Li, D. Guo, C. Li, A. Liu and H. Bai, *ACS Nano*, 2019, **13**, 7930–7938.
23 X. Zhao, H. Zhang, K.-Y. Chan, X. Huang, Y. Yang and X. Shen, *Nano-Micro Lett.*, 2024, **16**, 222.
24 Y. Guo, H. Lu, F. Zhao, X. Zhou, W. Shi and G. Yu, *Adv. Mater.*, 2020, **32**, e1907061.
25 F. Z. X. Zhou, Y. Guo, B. Rosenberger and G. Yu, *Sci. Adv.*, 2019, **5**, eaaw5484.
26 X. Zhou, F. Zhao, Y. Guo, Y. Zhang and G. Yu, *Energy Environ. Sci.*, 2018, **11**, 1985–1992.
27 R. Niu, J. Ren, J. J. Koh, L. Chen, J. Gong, J. Qu, X. Xu, J. Azadmanjiri and J. Min, *Adv. Energy Mater.*, 2023, **13**, 2302451.
28 J. Wang, X. Cao, X. Cui, H. Wang, H. Zhang, K. Wang, X. Li, Z. Li and Y. Zhou, *Adv. Mater.*, 2024, **36**, 2311151.
29 M. Zhang, K. Sun, Z. Zheng, H. Liu and X. Wang, *Desalination*, 2023, **550**, 116380.
30 H. Shen, Z. Zheng, H. Liu and X. Wang, *J. Mater. Chem. A*, 2022, **10**, 25509–25526.
31 M. S. Irshad, N. Arshad, J. Zhang, C. Song, N. Mushtaq, M. Alomar, T. Shamim, V.-D. Dao, H. Wang, X. Wang and H. Zhang, *Adv. Energy Sustainability Res.*, 2023, **4**, 2200158.
32 J. Yang, Y. C. Zhou, L. Y. Yang, C. P. Feng, L. Bai, M. B. Yang and W. Yang, *Adv. Funct. Mater.*, 2022, **32**, 2200792.
33 X.-Y. Wang, J. Xue, C. Ma, T. He, H. Qian, B. Wang, J. Liu and Y. Lu, *J. Mater. Chem. A*, 2019, **7**, 16696–16703.
34 X. Han, S. Ding, L. Fan, Y. Zhou and S. Wang, *J. Mater. Chem. A*, 2021, **9**, 18614–18622.
35 H. Xu, H. Xing, S. Chen, Q. Wang, L. Dong, K. D. Hu, B. Wang, J. Xue and Y. Lu, *Nanoscale*, 2022, **14**, 7493–7501.
36 J. Xue, H. L. Gao, X. Y. Wang, K. Y. Qian, Y. Yang, T. He, C. He, Y. Lu and S. H. Yu, *Angew. Chem., Int. Ed.*, 2019, **58**, 14152–14156.
37 W. Ma, T. Lu, W. Cao, R. Xiong and C. Huang, *Adv. Funct. Mater.*, 2023, **33**, 2214157.
38 E. Kim, K.-Y. Chan, J. Yang, H. Venkatesan, M. H. Adegun, H. Zhang, J.-H. Lee, X. Shen and J.-K. Kim, *J. Mater. Chem. A*, 2023, **11**, 7105–7114.
39 M. H. Adegun, K.-Y. Chan, J. Yang, H. Venkatesan, E. Kim, H. Zhang, X. Shen, J. Yang and J.-K. Kim, *Composites, Part A*, 2023, **169**, 107522.
40 K.-Y. Chan, X. Shen, J. Yang, K.-T. Lin, H. Venkatesan, E. Kim, H. Zhang, J.-H. Lee, J. Yu and J. Yang, *Nat. Commun.*, 2022, **13**, 5553.
41 Q. Yan, R. Ding, H. Zheng, P. Li, Z. Liu, Z. Chen, J. Xiong, F. Xue, X. Zhao, Q. Peng and X. He, *Adv. Funct. Mater.*, 2023, **33**, 2301982.
42 L. Zhang, J. Zhao, J. Zhu, C. He and H. Wang, *Soft Matter*, 2012, **8**, 10439–10447.
43 Y. Shi, D. Xiong, J. Li and N. Wang, *J. Phys. Chem. C*, 2016, **120**, 19442–19453.
44 Y. Zhang, G. Zhang, Z. Ma, J. Qin and X. Shen, *Nano Res.*, 2024, 1–11.
45 X. Shen, Z. Wang, Y. Wu, X. Liu, Y.-B. He, Q. Zheng, Q.-H. Yang, F. Kang and J.-K. Kim, *Mater. Horiz.*, 2018, **5**, 275–284.
46 X. Shen, Z. Wang, Y. Wu, X. Liu and J.-K. Kim, *Carbon*, 2016, **108**, 412–422.
47 Y. Lin, Q. Kang, H. Wei, H. Bao, P. Jiang, Y. W. Mai and X. Huang, *Nano-Micro Lett.*, 2021, **13**, 180.

